Theoretical and Applied Fracture Mechanics 125 (2023) 103940

Contents lists available at ScienceDirect

Theoretical and Applied Fracture Mechanics

journal homepage: www.elsevier.com/locate/tafmec

Numerical prediction of warm pre-stressing effects for a steam turbine steel

Ahmed Azeez [a,*], Daniel Leidermark [a], Mikael Segersäll [b], Robert Eriksson [a]

[a] Division of Solid Mechanics, Department of Management and Engineering, Linköping University, SE-581 83 Linköping, Sweden
[b] Division of Engineering Materials, Department of Management and Engineering, Linköping University, SE-581 83 Linköping, Sweden

ARTICLE INFO

Keywords:
Fracture toughness
Warm pre-stressing
Fracture mechanics
High temperature steel
Finite element analysis

ABSTRACT

In warm pre-stressing (WPS), the fracture resistance of cracked steel components is raised when subjected to certain temperature-load histories. WPS's beneficial effects enhance safety margins and potentially prolong fatigue life. However, understanding and predicting the WPS effects is crucial for employing such benefits. This study utilised pre-cracked compact tension specimens made from steam turbine steel for WPS and baseline fracture toughness testing. Two typical WPS cycles were investigated (L-C-F and L-U-C-F), and an increase in fracture resistance was observed for both cycles. The WPS tests were simulated using finite element analysis to understand its effects and predict the increase in fracture resistance. A local approach was followed based on accumulative plastic strain magnitude ahead of the crack tip. Since cleavage fracture is triggered by active plasticity, the WPS fracture is assumed when accumulated plasticity exceeds the residual plastic zone formed at the crack tip due to the initial pre-load.

1. Introduction

An increase in the apparent fracture toughness can be observed in steels exposed to certain temperature-load histories. This phenomenon is referred to as warm pre-stressing (WPS), which occur when a material with a flaw or crack is pre-loaded at a high temperature, typically above its ductile–brittle transition temperature (DBTT), leading to an increase in the fracture resistance at lower temperatures, typically below the DBTT [1,2]. The WPS effects increase the stress intensity factor at fracture, making it above the fracture toughness of the material [3]. This increase in fracture resistance (due to WPS) does not alter the material's fracture toughness. However, it is a consequence of the load-temperature history from WPS that affected the stress field around the crack [4]. Several researchers acknowledged three distinct mechanisms influencing the WPS effects: blunting of the crack tip, development of residual stresses around the crack, and increase in yield strength due to crack tip work hardening [3,5,6]. In particular, residual stresses are thought to have the primary influence since stress-relief heat treatment was seen to lower the beneficial effects of WPS [5,7,8]. A WPS study on HSLA steel showed that crack tip blunting was the main mechanism in enhancing the fracture resistance while the local residual stresses were of secondary importance [9]. In another study, crack tip blunting was found to be the dominant mechanism at low and moderate levels of WPS pre-loading, whereas, at higher pre-loads, the primary influence was from the residual stresses [10]. In a separate study, the residual stresses and crack tip blunting mechanisms were insufficient to explain the increase in fracture resistance due to WPS, and the accumulation of equivalent plastic deformation was thought to induce cleavage resistance [11]. In a study including a large set of WPS tests, the change in the yield strength was argued to have an insignificant role [4]. In general, these three identified mechanisms behind the WPS effect could have a different level of influence. It is controversial which of them plays the major role. Nevertheless, all these three mechanisms can be seen as a consequence of the plastic deformation generated at the crack tip due to the initial WPS pre-loading. Any subsequent unloading after the initial pre-load is thought to cause resharpening of the crack tip leading to a drop in the beneficial effects of WPS [12]. In addition, time-dependent processes, such as strain ageing, have been observed to reduce or eliminate the WPS effects [4]. The conditions where no WPS beneficial effects were produced have also been investigated [13].

Different temperature-load history paths could be applied in a WPS test. Two common transients are the load-cool-fracture (L-C-F) cycle and load-unload-cool-fracture (L-U-C-F) cycle, which are widely used for investigating the WPS effects [2,14,15]. These two cycles of WPS can be thought of as two extreme cases which envelopes other WPS transients, where L-C-F gives the highest effect with the lowest scatter, and L-U-C-F gives the lowest effect with the highest scatter [4,15,16]. Using other types of cycles would produce a WPS effect that is somewhere between these two cycles, i.e. L-C-F and L-U-C-F [4,16]. Higher fracture resistance values in the L-C-F cycle compared to the L-U-C-F cycle have been confirmed in previous studies [2,7,14].

* Corresponding author.
E-mail address: ahmed.azeez@liu.se (A. Azeez).

https://doi.org/10.1016/j.tafmec.2023.103940
Received 17 April 2023; Received in revised form 5 May 2023; Accepted 17 May 2023
Available online 20 May 2023

More complicated WPS load-temperature path variations have also been investigated [16,17], including partial unloading and reheating processes [3].

The beneficial effects of WPS have been mainly utilised to enhance the safety margins of nuclear reactor pressure vessels under critical conditions, e.g. in loss of coolant accidents and pressurised thermal shocks. Therefore, numerous studies have investigated the behaviour of WPS in reactor pressure vessel steels [3,5,17]. Limited studies have been carried out to investigate WPS effects on steam turbine steels. The beneficial effects of WPS can become relevant in prolonging the life of steam turbine components. Since flexible operations are required from steam turbines to support renewable energy systems, conservative and accurate fatigue life prediction models are needed, which include fatigue crack growth models [18,19]. Taking advantage of WPS effects would enhance the fracture resistance, allowing longer fatigue cracks to grow within safe limits before service overhaul. Understanding and predicting the WPS behaviour for steam turbine steels is necessary to achieve such benefits.

Both global and local approaches have been developed to predict the WPS effects. In global approaches, the stress–strain field ahead of the crack tip is not required, where a global parameter is used, such as Wallin model [4,20] and Chell model [21]. Wallin's model used a simple expression, based on the stress intensity factor, for predicting the WPS fracture load and was developed through the master curve approach using a large set of WPS data. A similar level of accuracy was shown between the Wallin model and the Chell model [4]. On the other hand, the local approaches require a detailed description of the stress–strain field at the crack tip and are typically based on the weakest link theory. Widely used local approaches include Beremin model [22], which was further developed into the modified Beremin model [3,23]. Jacquemoud and Nédélec [16] observed that the Beremin model was inadequate in accounting for unloading steps in WPS cycles; however, this issue could be related to their use of isotropic hardening in the finite element (FE) simulation. Local approaches generally take into consideration the loading history, which in some sense provides a physical representation of the fracture [12,16]. Local approaches are also advantageous for implementation in the numerical models of components and structures. Nevertheless, the global approaches can be desirable for their simplicity and ease of use; however, they are generally conservative in estimating the WPS fracture resistance [16].

The current study performed several WPS tests on a steam turbine steel called FB2, using both L-C-F and L-U-C-F cycles. Baseline fracture toughness tests were also carried out on the same steel at temperatures of 20–500 °C. The experimental data showed beneficial effects for all the WPS tests, i.e. increased apparent fracture resistance. Numerical simulations using FE analysis were performed for the WPS tests to predict their beneficial effects. A local approach based on the accumulated plastic strain ahead of the crack tip was followed for predicting the WPS fracture load of both L-C-F and L-U-C-F cycles. At the maximum WPS pre-load, the crack tip would experience plastic deformation leading to a residual plastic zone, often called the residual zone [15,21]. In the case where unloading is followed, e.g. in the L-U-C-F cycle, a change in the stress state would occur, and the accumulated plastic strain within the residual zone would reduce. During the WPS cycle, the residual zone would not increase further until plasticity is introduced again during the WPS fracture. It has been seen that the initiation of cleavage fracture requires the presence of active plasticity [7,12]. Thus, WPS failure should occur at the onset of accumulated plasticity exceeding the residual zone.

2. Material and experiments

2.1. Material and specimen

In this work, steam turbine steel known as FB2 (9Cr-1Mo-1Co-0.2V-0.07Nb-0.01B-0.02N, all in wt%) was utilised in all the experimental testing. This steel was the outcome of the European program of Co-operation in Science and Technology (COST) 522 (1998–2003), which aimed at improving 9–12% Cr steels for high-temperature steam turbine application [24–27]. The high resistance to creep and steam oxidation of the 9–12% Cr steel class made them desirable for use in steam turbine components subjected to high temperatures [27–32]. The FB2 steel has been utilised in the state-of-the-art steam turbine components due to its strong mechanical properties under harsh steam conditions with high pressure and temperature (up to 300 bar and 620 °C) [25–29]. A tempered martensitic microstructure was observed for the FB2 steel in the investigations performed by Azeez et al. [33] on the same batch of the FB2 steel tested in the current work. The FB2 steel underwent a heat treatment process of austenitisation at a very high temperature of 1100 °C with rapid cooling and followed by two tempering stages at 570 °C and 720 °C [25,28,29].

2.2. Specimen and testing rig

The experimental tests, fracture toughness and warm pre-stressing, were performed on compact tension (CT) specimens with side grooves. Fig. 1 (a) shows a three-dimensional schematic view of the CT specimen with side grooves where the parameters B, B_{N}, W, and a are specimen's thickness, the side groove thickness, the width, and the crack length, respectively. As shown, the crack length, a, is measured from the load line position (centre of the holes), and it includes both the crack starter and the sharp crack. The CT specimen was manufactured by machining the outer dimensions and drilling the holes. At the same time, the detailed profile, including the crack starter and the side grooves, was created through electrical discharge machining. No other surface finishing processes were applied. A detailed specimen drawing can be seen in Fig. 1(b). The manufactured crack starter had a length of about 22 mm, see Fig. 1, and it helped initiate the sharp crack during the pre-cracking process. A crack length of about $a \approx 25$ mm was aimed during the pre-cracking process, i.e. sharp crack length of about ∼ 3 mm; however, a more accurate value of the pre-crack length was measured post-fracture. For CT specimens with side grooves, the mode-I stress intensity factor, K, can be found in literature and is given by [34,35]

$$K = \frac{F}{\sqrt{BB_{\mathrm{N}}W}} \frac{2 + \frac{a}{W}}{\left(1 - \frac{a}{W}\right)^{\frac{3}{2}}} \left[0.886 + 4.64\frac{a}{W} - 13.32\left(\frac{a}{W}\right)^2 + 14.72\left(\frac{a}{W}\right)^3 - 5.6\left(\frac{a}{W}\right)^4 \right] \quad (1)$$

where F is the applied force on the CT specimen.

The 100 kN Alwetron electromechanical test frame, shown in Fig. 2, was used for both fracture toughness and warm pre-stressing testing. The testing rig included a 3-zone split furnace, and the temperature was controlled using three thermocouples. A thermocouple was attached to each grip while the third thermocouple was connected to the side of the mounted CT specimen, see Fig. 2. The displacement was measured along the load line using a high-temperature extensometer from Epsilon Technology Corporation.

2.3. Experimental testing

In this study, fracture toughness and WPS tests were performed on the CT specimen with side grooves. In the fracture toughness tests, the specimens were initially heated to the desired temperature and then loaded monotonically to fracture where the maximum fracture force, F_{frac}, was recorded. The tests were done in temperature, T, range of 20–500 °C. All the performed fracture toughness tests are presented in Table 1, where a is the crack length measured post-fracture, and K_{IC} is the stress intensity factor at fracture, i.e. fracture toughness, which corresponds to F_{frac} and calculated using Eq. (1). The fracture

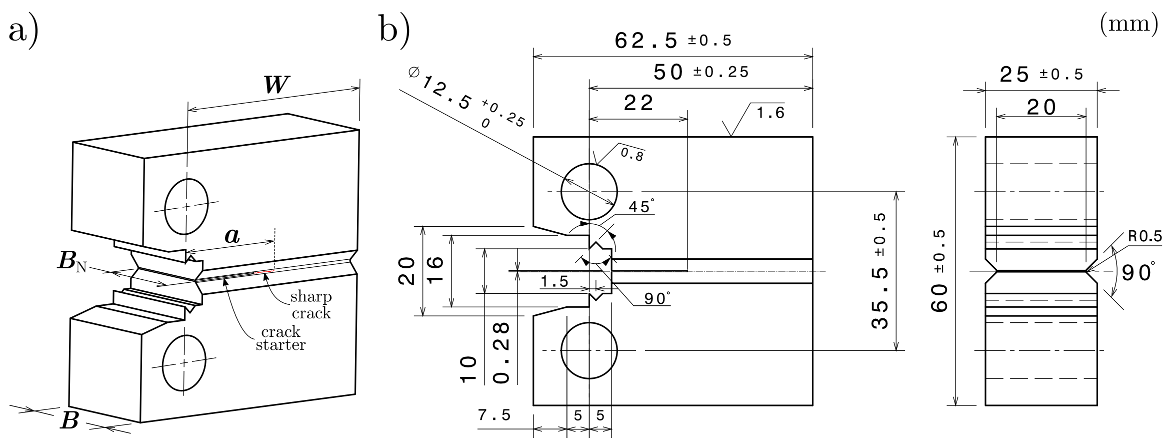

Fig. 1. Compact tension, CT, specimen used for fracture toughness and warm pre-stressing testing. (a) Three dimensional view showing the parameters W, B, B_N, and a. (b) Detailed drawing. The crack starter was manufactured, while the sharp crack was introduced by the pre-cracking procedure.

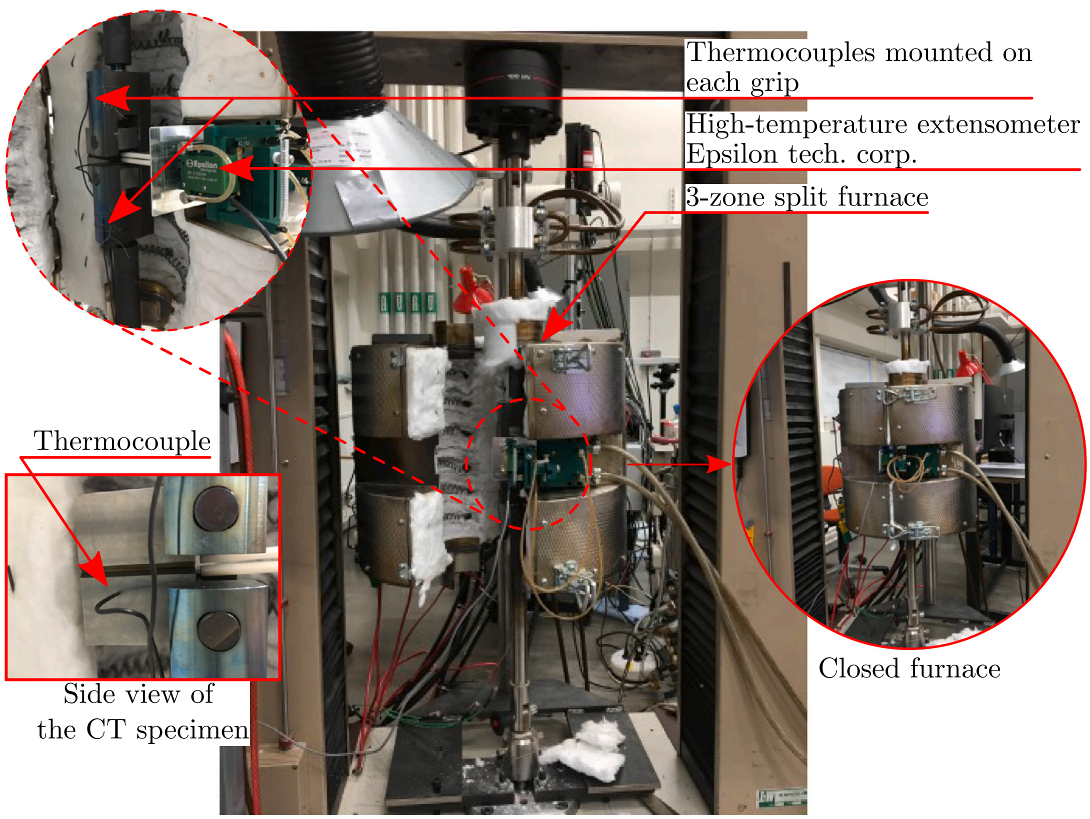

Fig. 2. Alwetron TCT 100, a 100 kN electromechanical test rig, with a 3-zone split furnace used for fracture toughness and warm pre-stressing testing.

toughness was based on the maximum fracture force, F_{frac}, to be consistent with the evaluation method used in WPS tests. For the WPS testing, the two common types of loading cycles were used, i.e. L-C-F and L-U-C-F. Fig. 3(a) and (b) shows schematic illustration of the L-C-F and the L-U-C-F cycles, respectively. In the L-C-F cycle (see Fig. 3(a)), the CT specimen was initially heated up to the maximum WPS temperature, T_{max}, then the WPS loading force, F_{ld}, (or stress intensity, K_{ld}) was applied during the loading step. The applied load (F_{ld} or K_{ld}) was held while the specimen was cooled down to the minimum WPS temperature, T_{min}. Finally, at T_{min}, the specimen was loaded to fracture where the fracture force, F_{frac}, (or stress intensity, K_{frac}) was recorded. On the other hand, in the L-U-C-F cycle (see Fig. 3(b)), the specimen was heated to T_{max} and loaded to F_{ld} (or K_{ld}) similarly to the loading step in the L-C-F cycle; however, this was followed by unloading to the WPS unloading force, F_{unld}, (or stress intensity, K_{unld}) at the same temperature of T_{max}. The unloading force was similar for all tests with L-U-C-F cycles, i.e. $F_{unld} = 0.5$ kN. Then, after cooling down to T_{min}, the specimen was loaded to fracture where F_{frac} (or K_{frac}) was recorded. All the stress intensity factors shown, i.e. K_{ld}, K_{unld}, and K_{frac}, were computed using the corresponding forces, i.e. F_{ld}, F_{unld}, and F_{frac}, respectively, and the corresponding crack length, a, through Eq. (1). Table 2 shows all the performed WPS tests and the recorded fracture data. The maximum WPS temperature, T_{max}, used were 100–400 °C and the minimum WPS temperature, T_{min}, used were 20 °C and 50 °C, while the loading forces, F_{ld}, used were 40–60 kN.

For each tested specimen, a slight pre-load of 0.5 kN was applied prior to the heating to prevent the specimen from going into compression during the heating process. To ensure homogeneous temperature

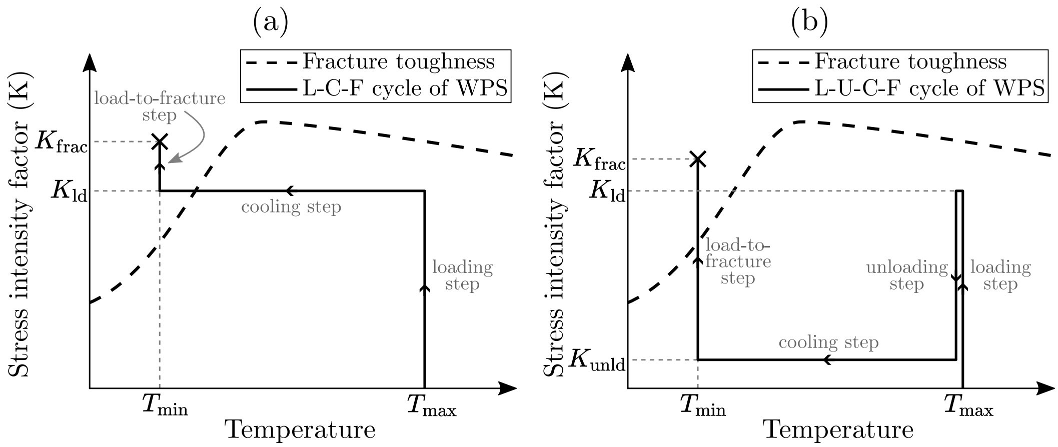

Fig. 3. Warm pre-stressing (WPS) types of loading cycles: (a) load-cool-fracture, L-C-F; (b) load-unload-cool-fracture, L-U-C-F. The maximum and minimum WPS temperatures are denoted by T_{max} and T_{min}, respectively. The stress intensity factors at loading, unloading, and fracture are denoted K_{ld}, K_{unld}, and K_{frac}, respectively.

Table 1
Fracture toughness tests performed on the FB2 steel within this work.

Specimen	T, °C	a, mm	F_{frac}, kN	K_{IC}, MPa$\sqrt{m}$
FT-01	20	25.19	30.67	59.96
FT-02	50	25.00	45.16	87.24
FT-03	100	25.05	69.97	135.61
FT-04	200	24.69	80.83	153.21
FT-05	300	24.74	76.00	144.52
FT-06	400	25.37	68.52	135.41
FT-07	500	25.09	65.10	126.43

distribution within the specimen, a 30 min dwell duration at the desired temperature was allowed. In the fracture toughness tests, the furnace was shut down after the specimen was pulled to fracture. In the WPS tests with T_{min} = 20 °C, for the L-C-F cycle, the furnace was shut down directly after reaching F_{ld} (or K_{ld}), while for the L-U-C-F cycle, the furnace was shut down directly after unloading to F_{unld} (or K_{unld}). In WPS tests with T_{min} = 50°C, the furnace was set to 50 °C instead of shutting it down. For all WPS tests, the specimens were left to completely cool down to T_{min} in the furnace overnight. A cross-head displacement control of 1 mm/min was utilised for pulling the specimens to fracture in both the fracture toughness and the WPS tests. After the fracture, measurements of the final crack length were done on each side of the crack surface, and an average value, a, was computed and reported in Tables 1 and 2 [34]

3. Experimental results

All the experimental WPS tests survived the cooling step from the maximum WPS temperature, T_{max}, to the minimum WPS temperature, T_{min}. After the cooling process, additional loading above the WPS loading force, F_{ld}, was possible for all the WPS tests. The stress intensity factor versus temperature for all the WPS tests, along with the monotonic fracture toughness tests, are shown in Fig. 4. In Fig. 4(a) and (b), WPS tests with L-C-F cycle are shown for T_{min} of 20 °C and 50 °C, respectively. In Fig. 4(c), WPS tests with L-U-C-F cycle are displayed (using T_{min} = 20 °C). The DBTT for the FB2 steel can be observed from the fracture toughness data in Fig. 4, where it occurs somewhere between 100–200 °C. For the WPS tests, the increase in the fracture resistance (K_{frac}) shows dependency on both T_{max} and F_{ld} (or K_{ld}) along with the dependency on the type of WPS cycle chosen, i.e. L-C-F or L-U-C-F. On the other hand, little to no dependency on T_{min} could be seen as similar values of K_{frac} was observed between Fig. 4(a) and (b) when using the same T_{max} and F_{ld} (or K_{ld}).

The increase in the apparent fracture resistance due to WPS effects can be observed clearly in Fig. 5 and Fig. 6 for L-C-F and L-U-C-F cycles, respectively. Figs. 5(a) and 6(a) shows K_{frac} versus T_{max}, while Figs. 5(b) and 6(b) shows K_{frac} versus F_{ld}. The stress intensity factor at fracture, K_{frac}, for all WPS tests, surpassed the fracture toughness performed at the corresponding minimum WPS temperature, T_{min}. As shown in Fig. 5(a) the use of higher T_{max} produced higher K_{frac} for the L-C-F cycle. However, the L-U-C-F cycle no such dependency can be observed between K_{frac} and T_{max}; see Fig. 6(a). On the other hand, similar behaviour between the L-C-F and L-U-C-F cycles could be observed in Figs. 5(b) and 6(b) where higher F_{ld} gives higher K_{frac}. The degree of dependency of K_{frac} on F_{ld} for the L-C-F cycle is larger compared to the dependency on T_{max}; see Fig. 5(a) and (b). Furthermore, almost no difference in K_{frac} could be seen among the WPS tests with different T_{min}, i.e. 20 °C and 50 °C; see Fig. 5(a). By comparing the L-C-F cycle to the L-U-C-F cycle, it can be observed that K_{frac} is generally higher for the L-C-F cycle. The difference in K_{frac} between L-C-F and L-U-C-F cycles seem to reduced for tests with low F_{ld} as observed between Figs. 5(b) and 6(b).

4. Modelling of warm pre-stressing

Finite element (FE) simulations were used to predict the effects of the temperature-load history from the WPS tests. In total, 14 simulations of WPS tests were performed, including 9 simulations for the L-C-F cycle and 5 simulations for the L-U-C-F cycle (see Table 2). For the simulation of the L-C-F cycle, four different maximum WPS temperatures, T_{max}, were used, i.e. 100 °C, 200 °C, 300 °C, and 400 °C, while for the L-U-C-F cycle, three different T_{max} were used, i.e., 200 °C, 300 °C, and 400 °C. Two different minimum WPS temperatures, T_{min}, of 20 °C and 50 °C were used for the L-C-F cycle, while only one T_{min} of 20 °C was used for the L-U-C-F cycle. In addition, three different WPS loading forces, F_{ld}, were used, i.e., 40 kN, 50 kN, and 60 kN, at T_{max} = 300 °C, while only one F_{ld} of 50 kN was used for the rest of the T_{max} used.

4.1. Boundary conditions, loading, mesh, and material model

The CT specimen (shown in Fig. 1) was modelled using a two-dimensional FE model with plane-strain conditions through the FE software ABAQUS [36]. The modelled CT specimen with the applied boundary and loading conditions is shown in Fig. 7. Two reference nodes were created at the centre of each hole of the CT specimen. Reference node 1, RP1, was at the centre of the upper hole, while reference node 2, RP2, was at the centre of the lower hole. Each reference node was coupled to one hole such that RP1 was coupled to the upper half of the upper hole, while RP2 was coupled to the lower half of the lower hole; see Fig. 7(b). The motion of the reference node was coupled to

Table 2
Warm pre-stressing tests performed on the FB2 steel within this work.

Specimen	Type	T_{max}, °C	T_{min}, °C	F_{ld}, kN	F_{unld}, kN	a, mm	F_{frac}, kN	K_{frac}, MPa$\sqrt{m}$
WPSLCF-01	L-C-F	100	20	50	(no unloading)	25.20	52.52	102.75
WPSLCF-02	L-C-F	200	20	50	(no unloading)	24.66	54.15	102.42
WPSLCF-03	L-C-F	300	20	40	(no unloading)	24.88	45.56	87.38
WPSLCF-04.1	L-C-F	300	20	50	(no unloading)	25.15	56.28	109.77
WPSLCF-04.2	L-C-F	300	20	50	(no unloading)	25.10	56.64	110.08
WPSLCF-05	L-C-F	300	20	60	(no unloading)	24.84	66.17	126.62
WPSLCF-06	L-C-F	400	20	50	(no unloading)	25.13	58.65	114.22
WPSLCF-07	L-C-F	200	50	50	(no unloading)	24.75	54.04	102.81
WPSLCF-08	L-C-F	300	50	50	(no unloading)	24.74	56.06	106.57
WPSLCF-09	L-C-F	400	50	50	(no unloading)	24.85	59.58	114.03
WPSLUCF-01	L-U-C-F	200	20	50	0.5	25.02	46.93	90.77
WPSLUCF-02	L-U-C-F	300	20	40	0.5	24.96	44.19	85.15
WPSLUCF-03	L-U-C-F	300	20	50	0.5	24.65	53.25	100.72
WPSLUCF-04	L-U-C-F	300	20	60	0.5	24.98	59.58	114.97
WPSLUCF-05	L-U-C-F	400	20	50	0.5	24.80	45.89	87.58

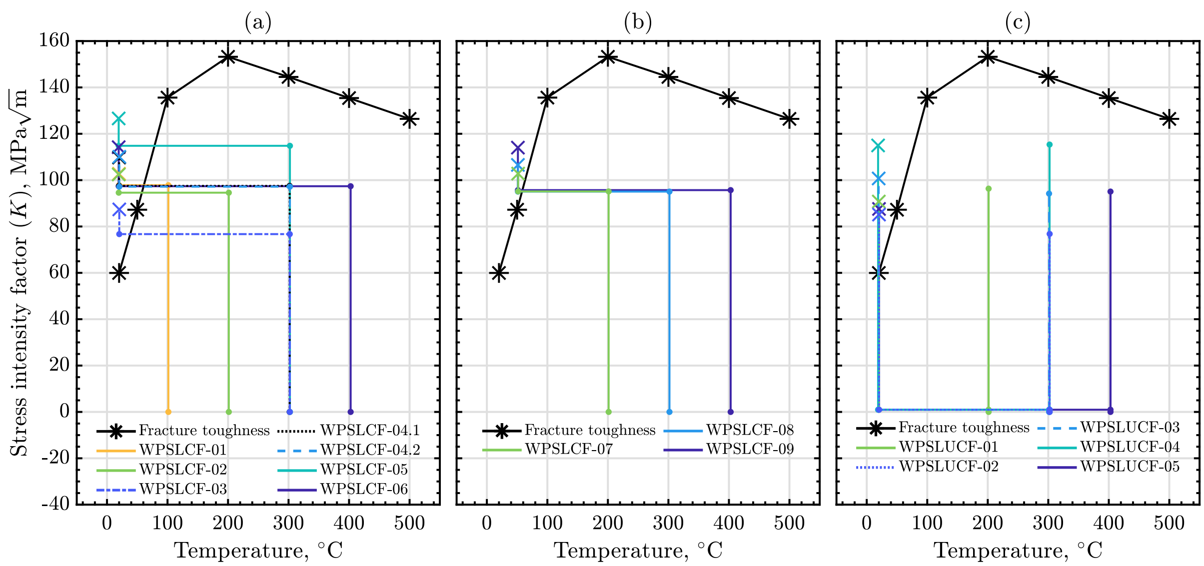

Fig. 4. Stress intensity factor versus temperature for the experimental WPS tests with: (a) L-C-F cycle and T_{min} = 20 °C; (b) L-C-F cycle and T_{min} = 50 °C; (c) L-U-C-F cycle and T_{min} = 20 °C. The (×) marker represent K_{frac}, i.e. the stress intensity at fracture.

the average motion of the coupling nodes on the coupled surfaces using the structural coupling method (see Fig. 7(b)) [36]. In addition, the coupling constraint is allowed to move along small patches of coupling nodes, making it suitable for cases with bending. Further details about the structural coupling method are available in the ABAQUS User's Manual [36].

The boundary conditions and the loading were applied on the CT specimen through the reference nodes, see Fig. 7(a). Fixed boundary conditions in X and Y directions were applied to reference node 2, RP2, during the simulation. On reference node 1, RP1, the displacement was fixed in the X direction, while the mechanical load was applied in the Y direction on the specimen through RP1 as a concentrated load. All the simulations included a sharp stationary crack inserted after the crack starter to represent the sharp crack created from the pre-cracking process; see the zoomed section of Fig. 7(a) and see Fig. 1(a). The sharp crack was created by inserting a line of length, l_{sharp}, and duplicating all the nodes along this line (except for the node at the tip) to form two sets of nodes on each side of the crack. All the performed FE simulations used a sharp crack length of l_{sharp} = 3 mm. Together with the crack starter length, i.e. 22 mm (see Fig. 1(b)), the desired final crack length of a = 25 mm was achieved. The use of a = 25 mm for all FE simulations was considered acceptable even though the actual tests showed slight variation in a, as seen in Table 2.

The CT specimen was meshed using structured 8-nodded quadratic plane-strain quadrilateral elements with reduced integration. The meshed specimen is shown in Fig. 8 with a zoomed view showing the mesh refinement done close to the crack starter and around the tip of the sharp crack. The mesh around the crack tip is defined as discussed in Ref. [18], i.e. contour mesh, where the quadratic quadrilateral elements around the tip (at the centre) were collapsed into a 6-nodded quadratic plane-strain modified triangle elements. All the collapsed nodes shared the same geometrical position (i.e. the crack tip) and were constrained together as a single node, while the mid-side nodes were moved so they were 30% away from the collapsed nodes. This procedure was done to improve the crack tip singularity.

The FE simulations used an elasto-plastic material model through the built-in constitutive models provided by the FE software ABAQUS [36]. The material model consisted of linear elastic and nonlinear kinematic hardening models with double backstresses. Von Mises yield criteria and associated flow rule were used. The evolution law of the nonlinear hardening model consisted of Ziegler's kinematic hardening law and a relaxation term (recall term) for each backstress, $\boldsymbol{\alpha}_m$, such [36]

$$\dot{\boldsymbol{\alpha}}_m = C_m \frac{\boldsymbol{\sigma} - \boldsymbol{\alpha}}{\sigma_y} \dot{\bar{\varepsilon}}^{p} - \gamma_m \boldsymbol{\alpha}_m \dot{\bar{\varepsilon}}^{p} \tag{2}$$

and the overall backstress tensor was

$$\boldsymbol{\alpha} = \sum_{m=1}^{2} \boldsymbol{\alpha}_m \tag{3}$$

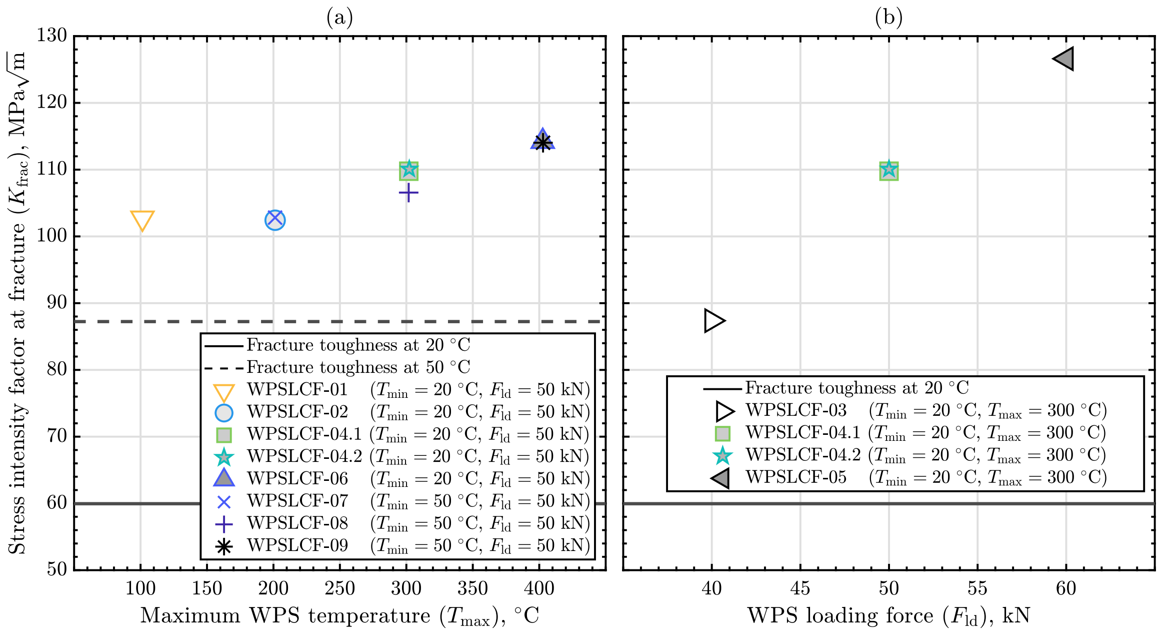

Fig. 5. Stress intensity factor at fracture, K_{frac}, for WPS tests with L-C-F cycle versus: (a) maximum WPS temperature, $T_{\max}$; (b) WPS loading force, F_{ld}. The solid and dashed lines represent the fracture toughness, K_{IC}, at 20 °C and 50 °C, respectively.

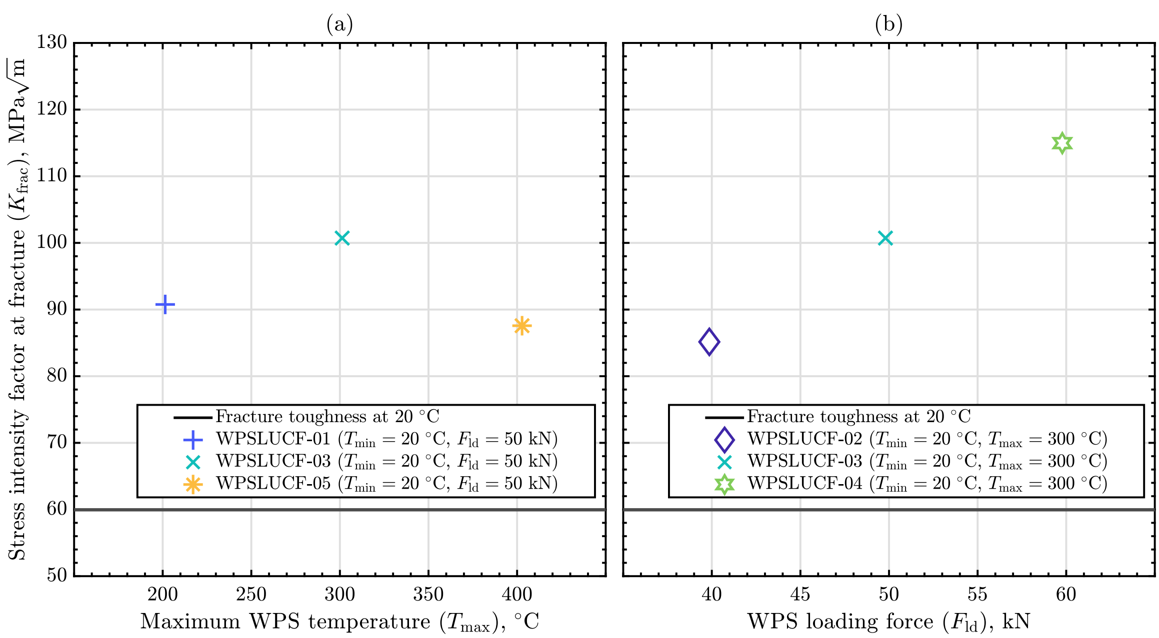

Fig. 6. Stress intensity factor at fracture, K_{frac}, for WPS tests with L-U-C-F cycle versus: (a) maximum WPS temperature, $T_{\max}$; (b) WPS loading force, F_{ld}. The solid lines represent the fracture toughness, K_{IC}, at 20 °C.

with C_m and γ_m being temperature-dependent material parameters with $m = 1, 2$. The parameters $\dot{\boldsymbol{\alpha}}_m$, $\boldsymbol{\sigma}$, σ_y, and $\dot{\bar{\varepsilon}}^{\mathrm{p}}$ are the rate of the backstress tensor, stress tensor, yield strength, and equivalent plastic strain rate, respectively.

All the temperature-dependent material parameters utilised in the current work were extracted from the initial cycle of isothermal low cycle fatigue tests performed in a previous work by Azeez et al. [33]. In these isothermal low cycle fatigue tests, smooth cylindrical specimens made from the same material batch of FB2 steel were used. The elasto-plastic model parameters used here were for the initial cyclic behaviour, which are provided and explained in detailed by Azeez et al. [18,19]. Table 3 shows the used material parameters, where E, ν, and $\Delta\varepsilon_{\mathrm{mec}}$ are elastic modulus, Poisson's ratio, and mechanical strain range of the isothermal low cycle fatigue tests Azeez et al. [18,19]. The material parameters were inserted into the FE model for every 10 °C over the temperature range 50–600 °C. Even though the simulations were performed for temperatures in the range of 20–400 °C, material parameters above 400 °C were used to produce a better interpolation fit for the desired temperature range. A creep model was not included in the FE model as the FB2 steel has shown little to no creep dependency for temperatures at and below 400 °C [33].

4.2. Numerical prediction of warm pre-stressing (WPS)

Several FE models were built as described in Section 4.1 and used to numerically predict the fracture load, F_{frac}, and the stress intensity

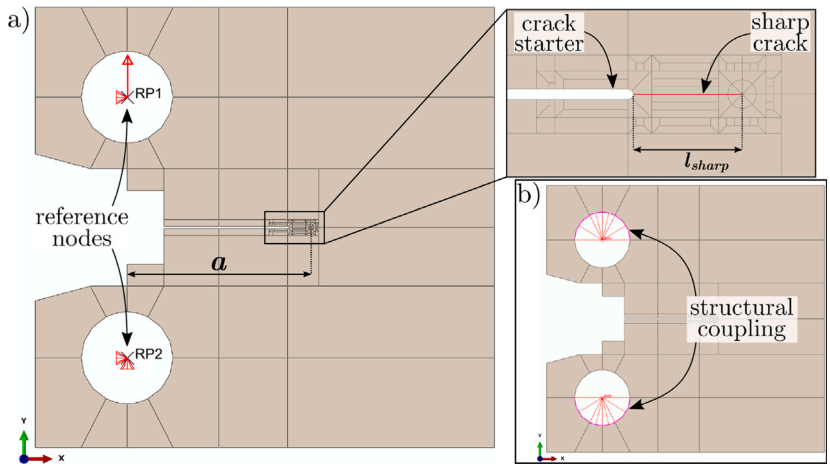

Fig. 7. The 2-dimensional FE modelled view of the compact tension, CT, specimen showing: (a) reference nodes where boundary conditions and loading is applied, while the zoomed view shows the crack starter and the sharp crack; (b) structural coupling applied between the reference node and the inner half circle edge of each specimen's hole. The parameter a is the crack length, while l_{sharp} is the length of the sharp crack.

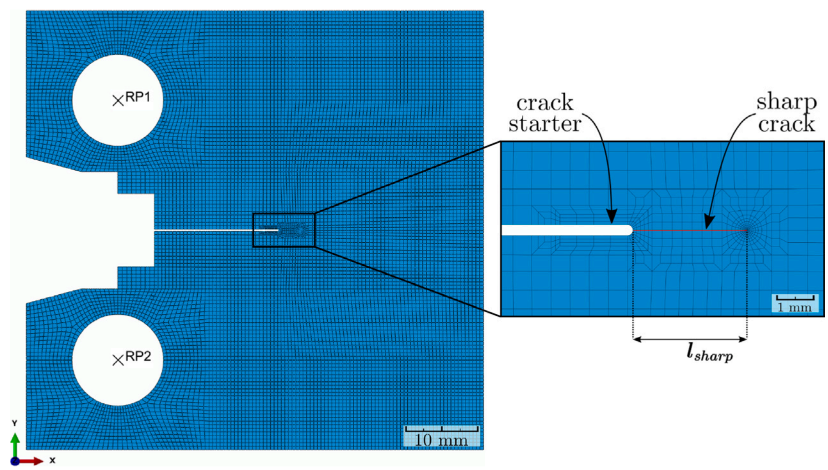

Fig. 8. The meshed view of the compact tension, CT, specimen. The zoomed view shows the mesh refinement close to the crack starter and around the tip of the sharp crack.

Table 3
Temperature-dependent material parameters for the elasto-plastic model of the steam turbine steel FB2 used for simulating the warm pre-stressing behaviour [18].

Temperature, °C	E, GPa	ν	$\Delta\varepsilon_{\mathrm{mec}}$, %	σ_y, MPa	C_1, MPa	C_2, MPa	γ_1	γ_2
20	213.97	0.285	2.0	588.40	44 680	322 985	426.07	4157.7
400	186.69	0.299	1.2	481.22	85 958	229 111	828.84	5821.7
500	179.91	0.305	1.2	420.31	101 264	257 438	870.96	5782.6
550	170.24	0.308						
600	159.41	0.312	1.2	300.20	118 360	584 880	1056.4	7054.7
625	147.36	0.314						

factor at fracture, K_{frac}, for the WPS tests (see Table 2). The models were set up to simulate both the L-C-F and L-U-C-F cycle of WPS (see Fig. 3). For all the simulations, the plastic strain magnitude, $\varepsilon_{\mathrm{p,mag}}$, was extracted from the nodes that lay on a straight line after the crack tip, i.e. along the ligament length. The plastic strain magnitude, $\varepsilon_{\mathrm{p,mag}}$, is accumulative measure that is derived from the plastic strain tensor, $\boldsymbol{\varepsilon}^{\mathrm{p}}$, and is given by [36]

$$\varepsilon_{\mathrm{p,mag}} = \sqrt{\frac{2}{3}\boldsymbol{\varepsilon}^{\mathrm{p}} : \boldsymbol{\varepsilon}^{\mathrm{p}}} \tag{4}$$

with $\boldsymbol{\varepsilon}^{\mathrm{p}} = \boldsymbol{\varepsilon} - \boldsymbol{\varepsilon}^{\mathrm{e}}$ where $\boldsymbol{\varepsilon}$, and $\boldsymbol{\varepsilon}^{\mathrm{e}}$ are total strain tensor, and elastic strain tensor, respectively. Fig. 9 shows the plastic strain magnitude, $\varepsilon_{\mathrm{p,mag}}$, versus the position ahead of the crack tip, X, for the FE simulation of WPSLCF-04 test (see Table 2). The values of $\varepsilon_{\mathrm{p,mag}}$ presented in the figure were taken at the end of the cooling step (see Fig. 3) where the applied force was 50 kN and temperature was 20 °C. In addition, Fig. 9 includes a schematic view of the crack starter and the sharp crack showing the crack tip point at $X = 0$ mm.

Using the plastic strain magnitude, $\varepsilon_{\mathrm{p,mag}}$, it was possible to compute the plastic zone size, r_{p}, through the FE simulations. By setting a small limit for the $\varepsilon_{\mathrm{p,mag}}$, as shown in Fig. 9, a corresponding position ahead of the crack tip is defined to be the plastic zone size, r_{p}. In the current work, the limit was set to be $\varepsilon_{\mathrm{p,mag}} = 0.1\%$, and the r_{p} was computed during the whole simulation for each FE model. The WPS fracture force, F_{frac}, was then found when the plastic zone size at fracture, $r_{\mathrm{p,frac}}$, is reached during the loading-to-fracture step (the last WPS loading step; see Fig. 3). In this study, the plastic zone size at fracture, $r_{\mathrm{p,frac}}$, is computed as

$$r_{\mathrm{p,frac}} = r_{\mathrm{p,C}} + 10\% \left(r_{\mathrm{p,C}}\right) \tag{5}$$

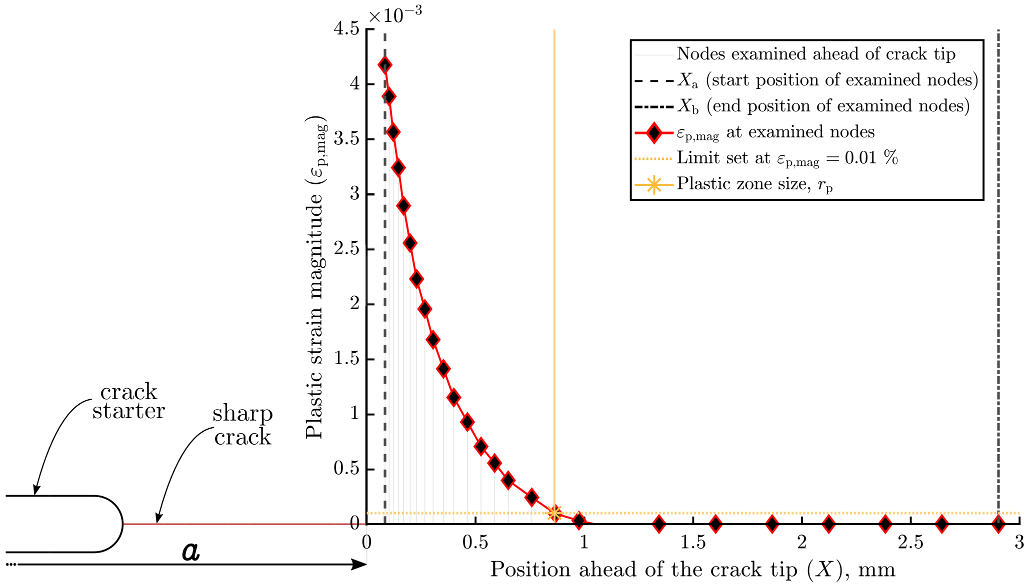

Fig. 9. An example of plastic strain magnitude, $\varepsilon_{p,mag}$, as a function of the position ahead of the crack tip, X, taken at the end of the cooling step for the FE simulated test WPSLCF-03. The diamond markers (⧫) are the examined nodes between X_a and X_b. A limit set of $\varepsilon_{p,mag} = 0.01\%$ (dotted line) was used to determined the FE estimated plastic zone size, r_p.

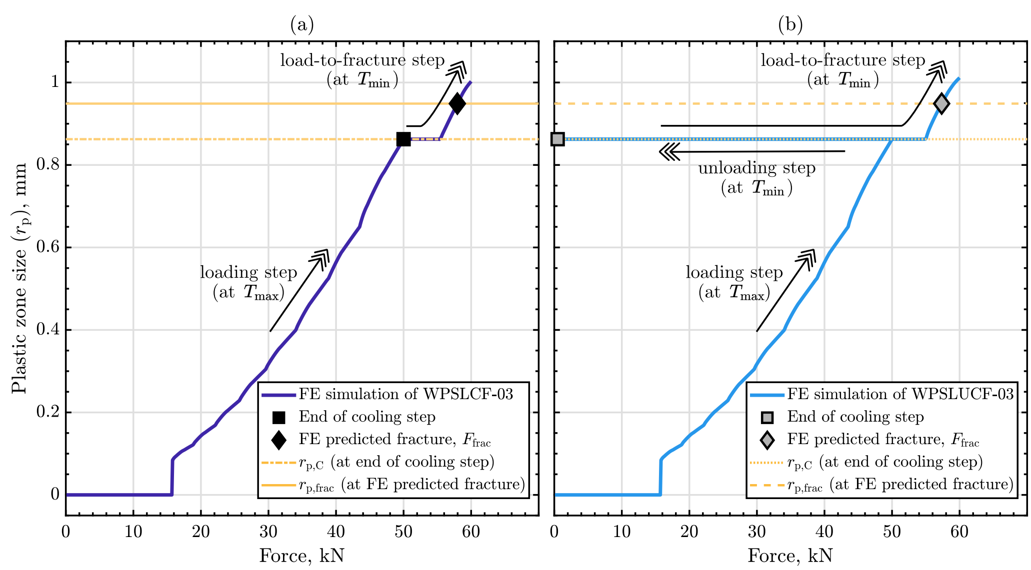

Fig. 10. An example of plastic zone size, r_p, as a function of the force for WPS tests with: (a) L-C-F cycle, from FE simulated test of WPSLCF-03, and (b) L-U-C-F cycle, from FE simulated test of WPSLUCF-03.

where $r_{p,C}$ is the plastic zone size at the end of the cooling step of the WPS tests (see Fig. 3). An example of r_p as a function of the applied force is shown in Fig. 10(a) and (b) for L-C-F (FE simulation of WPSLCF-03) and L-U-C-F (FE simulation of WPSLUCF-03) cycles, respectively. As implied in Eq. (5), the FE predicted fracture of the WPS is found when the plastic zone size becomes 10% bigger than the plastic zone size at the end of the cooling step, i.e. $r_{p,C}$ (see Fig. 10). For the L-C-F cycles, the end of the WPS cooling step is at a temperature of T_{min} and applied force of F_{ld}, while for the L-U-C-F cycle, it is at a temperature of T_{min} and applied force of F_{unld} (see Fig. 3).

Furthermore, a local parameter to estimate the amount of the accumulated plastic strain in front of the crack tip was proposed. This parameter, denoted by $\mathcal{P}_{int}$, is calculated by integrating the plastic strain magnitude, $\varepsilon_{p,mag}$, over a defined distance ahead of the crack tip, as

$$\mathcal{P}_{int} = \int_{X_a}^{X_b} \varepsilon_{p,mag}(X')\, dX' \tag{6}$$

where X_a is the position closest to the crack tip and X_b is the position far from the crack tip as shown in Fig. 9. The choice of X_a was slightly ahead of the crack tip (by skipping a couple of elements) to avoid unstable plastic strain magnitude values close to the crack tip singularity. Meanwhile, X_b was set to be far enough to include the largest plastic zone size during the simulation. In the current study, the choice of X_a was set to be after the 3rd element a head of the crack tip (from the 7th node a head of the crack tip), i.e. $X_a = 0.084$ mm, while $X_b = 2.9$ mm. The choice of X_a and X_b was the same for all the simulated FE models. After computing $\mathcal{P}_{int}$ for all the FE models, the WPS fracture force, F_{frac}, was predicted using a method similar to Eq. (5). The FE predicted WPS fracture force, F_{frac}, was found when the

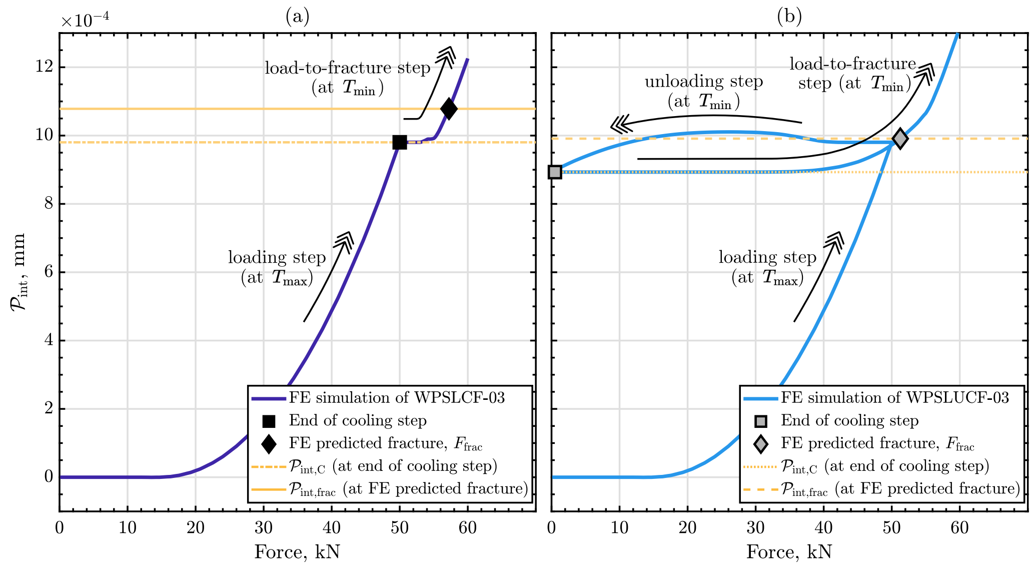

Fig. 11. An example of $\mathcal{P}_{int}$ as a function of force for WPS tests with: (a) L-C-F cycle, from FE simulated test of WPSLCF-03, and (b) L-U-C-F cycle, from FE simulated test of WPSLUCF-03.

integral parameter at fracture, $\mathcal{P}_{int,frac}$, was reached during the loading-to-fracture step. The integral parameter at fracture, $\mathcal{P}_{int,frac}$, is defined as

$$\mathcal{P}_{int,frac} = \mathcal{P}_{int,C} + 10\%(\mathcal{P}_{int,C}) \tag{7}$$

where $\mathcal{P}_{int,C}$ is the integral value at the end of the cooling step of the WPS tests (see Fig. 3). An example of $\mathcal{P}_{int}$ versus the applied force is shown in Fig. 11(a) and (b) for L-C-F (FE simulation of WPSLCF-03) and L-U-C-F (FE simulation of WPSLUCF-03) cycles, respectively. As presented in Eq. (7), the FE predicted fracture of the WPS is reached when $\mathcal{P}_{int}$ becomes 10% bigger than $\mathcal{P}_{int,C}$ found at the end of the cooling step.

The FE predicted stress intensity factor at fracture, K_{frac}, is found by substituting the FE predicted fracture force, F_{frac}, in the K solution of the CT specimen with side grooves, i.e. Eq. (1), along with the crack length used in the FE simulations, i.e. a = 25 mm. The stress intensity factor at fracture, K_{frac}, obtained from both the experimental and the FE simulated WPS tests are shown in Figs. 12 and 13 for the L-C-F and L-U-C-F cycles, respectively. The K_{frac} from the FE simulations were found using both the integral of the plastic strain magnitude, $\mathcal{P}_{int}$, and the plastic zone size, r_p. For the L-C-F cycle shown in Fig. 12, the FE predicted K_{frac} using the r_p and $\mathcal{P}_{int}$ show acceptable prediction to the experimental results. However, a slight improvement in the prediction can be seen when using the $\mathcal{P}_{int}$. For the L-U-C-F cycle shown in Fig. 13, the FE predicted K_{frac} using r_p shows poor prediction to the experimental data in comparison to the use of $\mathcal{P}_{int}$ where acceptable predictions can be seen.

5. Discussion

Through the use of a local prediction approach, the beneficial effects of WPS were observed to be primarily influenced by the residual plasticity generated at the crack tip due to the WPS pre-loading, i.e. WPS loading step (at K_{ld} and T_{max}, see Fig. 3). At the end of the WPS loading step, the plastic deformation ahead of the crack tip forms a residual plastic zone (or residual zone). Using the plastic zone size, r_p, as a local parameter, the size of this residual zone can be quantified, which is equal to $r_{p,C}$ for the L-C-F and L-U-C-F cycles as shown in Fig. 10(a) and (b). After the WPS loading step, no further increase in r_p can be observed until the final WPS loading-to-fracture step. The WPS fracture is assumed to occur when r_p increases beyond the size of the residual zone, indicating that active plasticity is taking place, which is required to initiate cleavage fracture [7,12]. The plastic zone size at fracture ($r_{p,frac}$) was calculated to be 10% bigger than the size of the residual zone; see Eq. (5) and Fig. 10. On the other hand, using $\mathcal{P}_{int}$, i.e. the integral of the plastic strain magnitude given in Eq. (6), as a local parameter, the amount of plasticity within the residual zone can be quantified. For the L-C-F cycle, as shown in Fig. 11(a), the plasticity within the residual zone due to the WPS pre-load, which is equal to $\mathcal{P}_{int,C}$, do not change until the final WPS loading-to-fracture step. This behaviour is similar between the two local parameters (r_p and $\mathcal{P}_{int}$) but only for the L-C-F cycle; see Figs. 10(a) and 11(a). In the L-U-C-F cycle, as shown in Fig. 11(b), the plasticity generated due to the WPS pre-load would eventually drop during the unloading step, where the accumulated residual plasticity after unloading is taken to be $\mathcal{P}_{int,C}$. The unloading step in the L-U-C-F cycle does not seem to reduce the residual zone size (see Fig. 10(b)); however, the amount of plasticity within that residual zone is reduced (see Fig. 11(b)). Then, with $\mathcal{P}_{int}$ parameter, the WPS fracture is set to take place when active plasticity ahead of the crack is introduced again during the load-to-fracture step. It is assumed to happen when $\mathcal{P}_{int}$ becomes 10% larger than $\mathcal{P}_{int,C}$, i.e. reaching $\mathcal{P}_{int,frac}$, for both L-C-F and L-U-C-F cycles; see Eq. (7) and Fig. 11. The use of the 10% in Eqs. (5) and (7) was found sufficient enough to produce a reasonable estimation for the WPS fracture load (K_{frac}) between the FE predictions and the experimental results; see Figs. 12 and 13. In addition, an FE simulation of the fracture toughness test at room temperature, i.e. FT-01 in Table 1, showed a similar level of plasticity ahead of the crack tip at the fracture compared to the 10% of plasticity allowed prior to the assumed WPS fracture.

In Figs. 12 and 13, the use of $\mathcal{P}_{int,frac}$ showed better prediction of K_{frac} to the experimental data than using $r_{p,frac}$, especially for the L-U-C-F cycle. A disadvantage of using the plastic zone size (r_p) as a local parameter is that it is insensitive to the change in the accumulated plastic strain magnitude for the nodes that lie within the plastic zone size ($X \leq r_p$); see Fig. 9. In contrast, the use of $\mathcal{P}_{int}$ quantifies the plasticity at the crack tip and provides insight into the development of plasticity for the whole region in front of the crack tip; see Eq. (6) and Fig. 9. The difference between these two local parameters ($\mathcal{P}_{int}$ and r_p) becomes most apparent when unloading occurs in the WPS tests, as in the L-U-C-F cycle (Fig. 3(b)), where r_p parameter is incapable of quantifying the reduction in plasticity ahead of the crack tip; see Figs. 10(b) 11(b). This behaviour could explain the significant difference in the prediction of K_{frac} between the two local parameters for the L-U-C-F cycle; see Fig. 13. Since better predictions were achieved through the

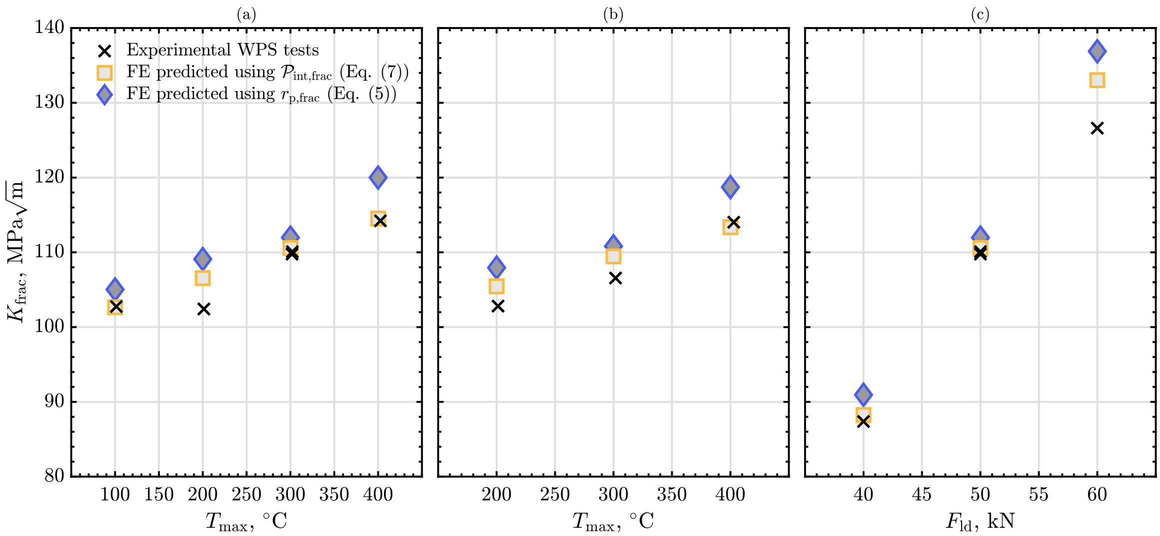

Fig. 12. The experimental and the FE predicted stress intensity factor at fracture, K_{frac}, is shown for the L-C-F cycle of WPS tests with: (a) T_{min} = 20 °C and F_{ld} = 50 kN; (b) T_{min} = 50 °C and F_{ld} = 50 kN; and (c) T_{min} = 20 °C and T_{max} = 300 °C. The FE predicted K_{frac} using $\mathcal{P}_{int,frac}$ and $r_{p,frac}$ can be seen.

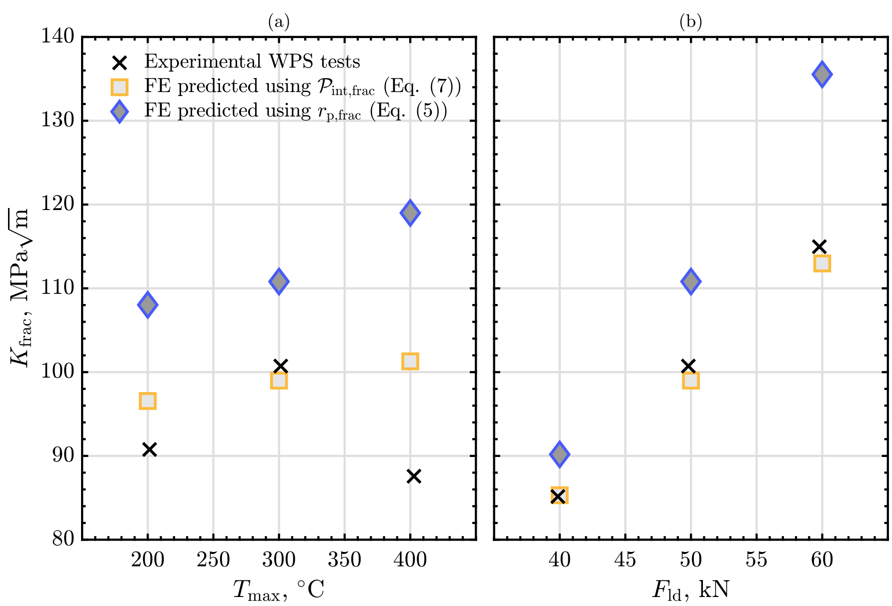

Fig. 13. The experimental and the FE predicted stress intensity factor at fracture, K_{frac}, is shown for the L-U-C-F cycle of WPS tests with: (a) T_{min} = 20 °C and F_{ld} = 50 kN; and (b) T_{min} = 20 °C and T_{max} = 300 °C. The FE predicted K_{frac} using $\mathcal{P}_{int,frac}$ and $r_{p,frac}$ can be seen.

use of $\mathcal{P}_{int}$, it can be seen that quantifying plasticity ahead of the crack tip and accounting for the reduction in plasticity during unloading is important. On the other hand, for WPS tests without unloading, as in the L-C-F cycle (see Fig. 3(a)), both of the local parameters showed a similar trend as seen in Figs. 10(a) and 11(a). This behaviour could be the reason behind the prediction of K_{frac} not showing a huge difference between r_p and $\mathcal{P}_{int}$ for the L-C-F cycle; see Fig. 12.

By observing Fig. 12(a) and (b), the stress intensity factor at fracture, K_{frac}, for the WPS tests with L-C-F cycle shows a clear dependency on the maximum WPS temperature, T_{max}, which was predicted reasonably well by the FE simulations using $\mathcal{P}_{int,frac}$. On the other hand, no clear dependency of K_{frac} on the minimum WPS temperature, T_{min}, could be observed. The dependency of K_{frac} on T_{max} is related to the different amounts of residual plastic deformation created at the crack tip during the WPS pre-load. By observing the WPS loading step shown in Fig. 14(a) and (b) (Fig. 11 shows the different WPS steps), it is clear that higher $\mathcal{P}_{int}$ is achieved with higher temperatures at the same WPS loading force, F_{ld} (WPS pre-load). During the load-to-fracture step, WPS tests with a higher amount of $\mathcal{P}_{int}$ (with the same F_{ld}), would require higher loads to introduce active plasticity necessary to initiate WPS fracture. It must be noted that the temperature dependency of $\mathcal{P}_{int}$ during the WPS loading step is directly related to the material mechanical properties being temperature dependent (see Table 3). Furthermore, since the material's elastic modulus and yield limit have both increased due to the WPS cooling step (temperature drop from T_{max} to T_{min}), the initial loading during the load-to-fracture step would not immediately generate plasticity at the crack tip. Higher residual plasticity at the crack tip means higher loads are needed to exceed the yield limit and produce active plasticity.

After plasticity is achieved during the WPS load-to-fracture step, further loading would produce $\mathcal{P}_{int}$ that coincides with FE simulation of monotonic loading at the same T_{min}, as shown in Fig. 14(a) and (b) for L-C-F cycle with T_{min} of 20 °C and 50 °C, respectively. Since the material mechanical properties between 20 °C and 50 °C are very similar, their monotonic loading curves are almost the same. Thus, the loading-to-fracture path for L-C-F cycle with T_{min} of 20 °C and 50 °C

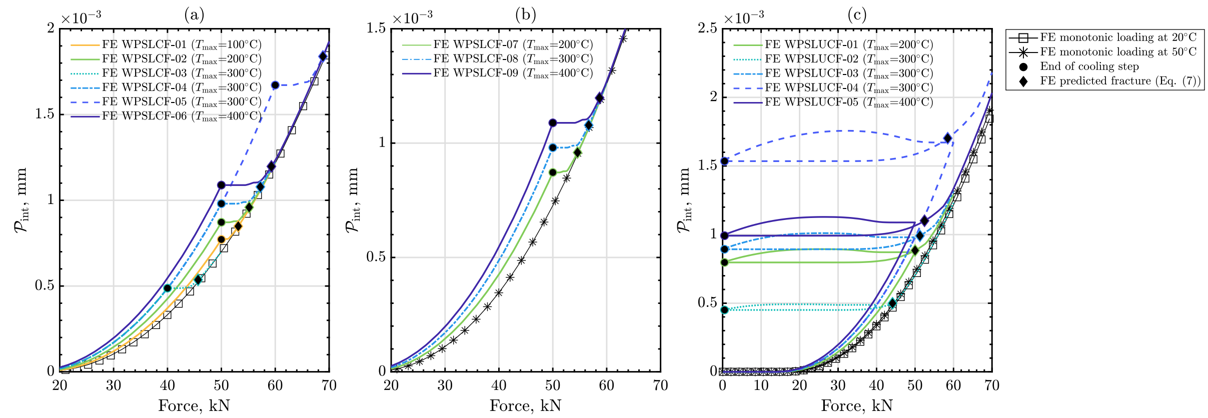

Fig. 14. The integral of the plastic strain magnitude a head of the crack tip, $\mathcal{P}_{\rm int}$, (see Eq. (6)) as a function of the applied force is shown for the FE simulations of WPS tests with: (a) L-C-F cycle and $T_{\rm min}$ = 20 °C; (b) L-C-F cycle and $T_{\rm min}$ = 50 °C; and (c) L-U-C-F cycle and $T_{\rm min}$ = 20 °C. FE simulations of monotonic loading at 20 °C and 50 °C are also presented.

would be very similar, explaining the weak dependency of $K_{\rm frac}$ on $T_{\rm min}$; see Fig. 12(a) and (b).

Moreover, in Fig. 12(c), a dependency of $K_{\rm frac}$ on $F_{\rm ld}$ can be seen for the L-C-F cycle. This behaviour is also related to residual plasticity generated at the crack tip during the WPS pre-load. Higher $F_{\rm ld}$ would produce higher residual plasticity for the same $T_{\rm max}$, which in turn leads to higher WPS fracture load; see Fig. 14(a).

For the L-U-C-F cycle, in Fig. 13(a), the experimental results show no clear dependence of $K_{\rm frac}$ on $T_{\rm max}$, which could be related to the somewhat large scatter that is known to happen for L-U-C-F cycles [15]. However, the FE prediction of $K_{\rm frac}$ using $\mathcal{P}_{\rm int,frac}$ present some dependency on $T_{\rm max}$, see Fig. 13(a). On the other hand, a dependency of $K_{\rm frac}$ on $F_{\rm ld}$ is observed in Fig. 13(b), which is well predicted using $\mathcal{P}_{\rm int,frac}$. As seen in Fig. 14(c), higher residual plasticity produced at the end of the cooling step would lead to higher force at the load-to-fracture step (higher $K_{\rm frac}$) to introduce the same amount of active plasticity ahead of the crack tip. The increase of $T_{\rm max}$ for the same $F_{\rm ld}$ has less effect on the amount of $\mathcal{P}_{\rm int}$ at the end of the cooling step, while higher $F_{\rm ld}$ provide higher effects; see Fig. 14(c). This behaviour is related to the level of plasticity created during the WPS pre-load, i.e. during the WPS loading step. The drop in $\mathcal{P}_{\rm int}$ due to the unloading step seems to show strong dependency on $F_{\rm ld}$, while less dependence can be seen for different $T_{\rm max}$; see Fig. 14(c). The loading during the load-to-fracture step in the L-U-C-F cycle does not initially produce any increase in $\mathcal{P}_{\rm int}$, similar to the L-C-F cycle. It can also be seen in Fig. 14(c) that additional loading, beyond the FE predicted fracture, would eventually increase $\mathcal{P}_{\rm int}$ to be parallel to the FE simulation of monotonic loading performed at $T_{\rm min}$. The increase in $T_{\rm max}$ and $F_{\rm ld}$ makes the final loading curve above the monotonic loading curve.

The WPS fracture force is generally higher for the L-C-F cycle compared to the L-U-C-F cycle. However, for low $F_{\rm ld}$ similar level of WPS fracture force is observed between the two cycles. This behaviour is related to the slight reduction in $\mathcal{P}_{\rm int}$ during the unloading step and the slow increase in active plasticity before following the monotonic loading curve during the load-to-fracture step. At higher $F_{\rm ld}$ in the L-U-C-F cycle, the opposite behaviour is seen, leading to lower $K_{\rm frac}$. Since higher residual plasticity produces higher $K_{\rm frac}$, it can be postulated that using higher $F_{\rm unld}$ for the L-U-C-F cycle would improve $K_{\rm frac}$ since the unloading step shows an increase in $\mathcal{P}_{\rm int}$ before the reduction begins; see unloading step in Fig. 14(c). However, further testing is required to confirm this assumption.

From Fig. 14, the estimation of the WPS fracture force, $F_{\rm frac}$, for the L-C-F cycle is possible without the need to perform FE simulation of the whole L-C-F cycle. It is enough by having only two FE simulations of simple monotonic loadings, one at $T_{\rm max}$ and another at $T_{\rm min}$. The $\mathcal{P}_{\rm int,C}$ is found from the WPS applied force, $F_{\rm ld}$ using the monotonic curve of $T_{\rm max}$. Then, the $\mathcal{P}_{\rm int,frac}$ is computed through Eq. (7), which is used to obtain $F_{\rm frac}$ through the monotonic curve of $T_{\rm min}$. This simple prediction method from Fig. 14(a) and (b) could be utilised for any parameters of the L-C-F cycle. In addition, more complicated WPS cycles could be predicted this way without simulating the entire cycle as long as no unloading occurs. However, further investigation of complicated L-C-F cycles is required to confirm this method. On the other hand, the unloading step introduces some complications for L-U-C-F cycles, which require the FE simulation of the entire cycle.

Furthermore, the FE simulations were also utilised to provide the WPS fracture load using the J-integral parameter, as shown in Fig. 15 (for the L-C-F cycle) and Fig. 16 (for the L-U-C-F cycle). The WPS fracture load predicted using the J-integral followed the same approach as the FE prediction using $\mathcal{P}_{\rm int,frac}$, i.e. Eq. (7), described in Section 4.2. However, it must be noted that due to the unloading step in the L-U-C-F cycle, the J-integral becomes path dependent [3]. Additionally, Figs. 15 and 16 included the WPS prediction model by Wallin [4], given by

$$
\begin{aligned}
&K_{\rm frac} = (0.15)\,K_{\rm IC} + \sqrt{K_{\rm IC}\left(K_{\rm ld} - K_{\rm unld}\right)} + K_{\rm unld} \\
&\quad \text{if} \quad K_{\rm unld} \geq K_{\rm ld} - K_{\rm IC} \quad \text{then set } K_{\rm unld} = K_{\rm ld} \\
&\quad \text{if} \quad K_{\rm frac} \leq K_{\rm IC} \qquad\quad\;\; \text{then set } K_{\rm frac} = K_{\rm IC}.
\end{aligned}
\tag{8}
$$

The prediction capacity of the Wallin model is fairly good for the L-C-F cycle, see Fig. 15, while it is conservative for the L-U-C-F cycle; see Fig. 16. The predictions by the J-integral are slightly better than the Wallin model for the L-C-F cycle, while it is the least conservative prediction method for the L-U-C-F cycle. The FE prediction method using $\mathcal{P}_{\rm int}$ presented the best prediction among the other methods for the L-C-F cycle, see Fig. 15. The Wallin model lacks the dependency on the maximum WPS temperature, $T_{\rm max}$, where almost constant values of $K_{\rm frac}$ are seen for different $T_{\rm max}$; see Fig. 15(a) and (b). For the L-U-C-F cycle, the experimental results in Fig. 16(a) could have a considerable scatter, where additional testing might be required to determine the accuracy of the different predictive methods. However, for Fig. 16(b), the FE prediction using $\mathcal{P}_{\rm int}$ provided the best prediction among the other methods.

Even though the WPS prediction approach developed in this study was based on the experimental data from a single steam turbine steel, i.e. FB2 steel, the approach should still be relevant for other steels. In addition, the experimental data produced are expected to be independent of the specimen geometry used, i.e. CT specimen. Future work to further explore the current WPS prediction approach is of interest, especially in exploring other types of WPS loading cycles.

6. Conclusions

Warm pre-stressing (WPS) tests were performed on compact tension specimens of a 9–12% Cr steam turbine steel called FB2. The

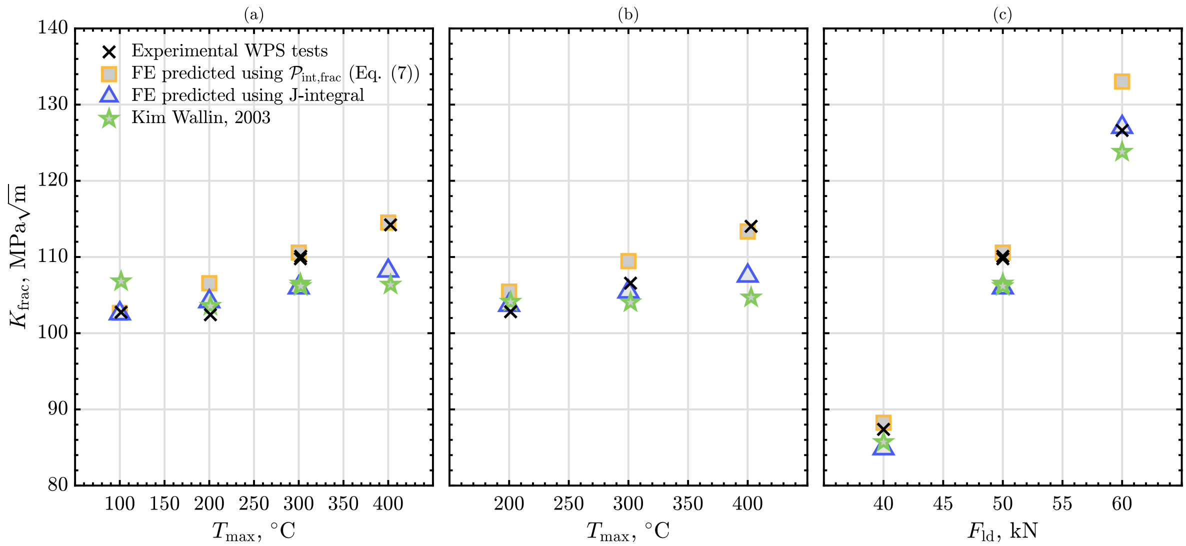

Fig. 15. The experimental and the FE predicted stress intensity factor at fracture, K_{frac}, is shown for the L-C-F cycle of WPS tests with: (a) T_{min} = 20 °C and F_{ld} = 50 kN; (b) T_{min} = 50 °C and F_{ld} = 50 kN; and (c) T_{min} = 20 °C and T_{max} = 300 °C. The FE predicted K_{frac} using $\mathcal{P}_{int,frac}$ and J-integral can be seen along with K_{frac} computed using Wallin [4] model.

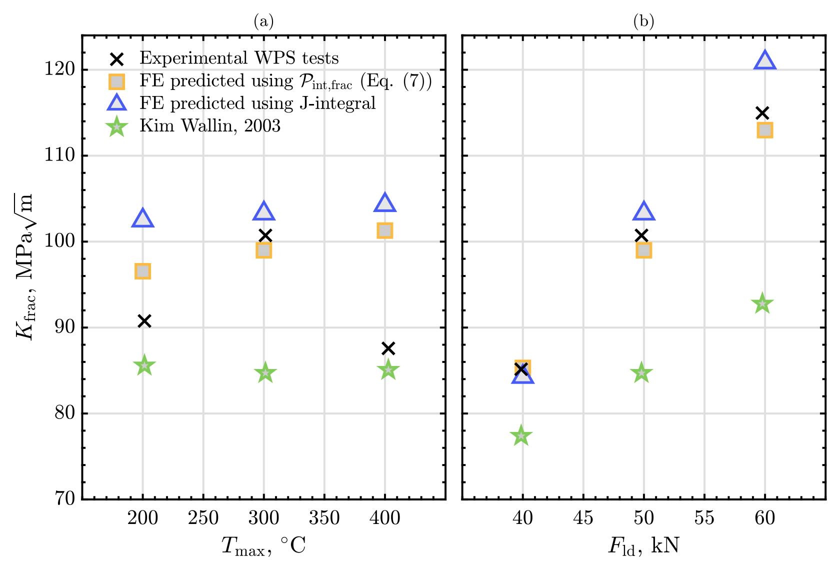

Fig. 16. The experimental and the FE predicted stress intensity factor at fracture, K_{frac}, is shown for the L-U-C-F cycle of WPS tests with: (a) T_{min} = 20 °C and F_{ld} = 50 kN; and (b) T_{min} = 20 °C and T_{max} = 300 °C. The FE predicted K_{frac} using $\mathcal{P}_{int,frac}$ and J-integral can be seen along with K_{frac} computed using Wallin [4] model.

effect of load-temperature history from the WPS tests was investigated, where two common types of WPS cycles were in focus, i.e. load-cool-fracture (L-C-F) and load-unload-cool-fracture (L-U-C-F). Baseline fracture toughness testing was also carried out for FB2 steel at different temperatures, i.e. 20–500 °C. Finite element (FE) analysis of two-dimensional models with plane-strain conditions was used to simulate all the WPS tests. Numerical prediction of the rise in the WPS fracture resistance was made based on the accumulated plastic strain magnitude computed ahead of the crack tip.

The following major conclusions drawn from this study are:

- All the WPS tests survived the cooling process, where an increase in fracture resistance due to WPS was observed for all the tests. The L-C-F cycle provided higher WPS fracture loads compared to the L-U-C-F cycle. However, this difference reduces with low WPS loading force.
- For the L-C-F cycle, the WPS fracture load (F_{frac} or K_{frac}) showed dependency on the maximum WPS temperature (T_{max}) used. However, such dependency was not seen for the L-U-C-F cycle, possibly due to the large scatter. A larger dependency of WPS fracture load on the WPS loading force (WPS pre-load) was observed for both L-C-F and L-U-C-F cycles.
- Numerical simulations could predict the WPS effects using the integral of the plastic strain magnitude, $\mathcal{P}_{int}$, as a local parameter to quantify plasticity at the crack tip. Using plastic zone size, r_p, as a local parameter, showed worst predictions, especially for the L-U-C-F cycle, due to the incapability of r_p to quantify the change in plasticity within the plastic zone, especially during the WPS unloading step. The utilised prediction approach assumes WPS fracture occurs when a reasonable level of active plasticity is introduced at the crack tip during the last WPS step (load-to-fracture step).

- The amount of residual plasticity produced at the crack tip from the WPS pre-load had a considerable influence on the WPS fracture load. After the WPS cooling step, the material's elastic modulus and yield limit would increase. Thus, large residual plasticity would require higher loads to produce active plasticity at the crack tip during the load-to-fracture step. The increase in maximum WPS temperature (T_{max}), as well as the increase in WPS loading force (F_{ld}), lead to high residual plasticity built after the cooling step. This behaviour explains the dependency of the WPS fracture load on T_{max} as well as on F_{ld}. Even for the L-U-C-F cycle, the FE prediction using $\mathcal{P}_{\mathrm{int,frac}}$ showed dependency on T_{max}. Quantifying the plasticity ahead of the crack tip and accounting for its change during any unloading step is necessary to produce good predictions for the WPS fracture load, which was done using the local parameter $\mathcal{P}_{\mathrm{int}}$.
- The numerical predictions of WPS fracture load using $\mathcal{P}_{\mathrm{int}}$ showed acceptable estimation to the experimental results. More accurate and less conservative predictions were observed compared to the Wallin model, which is based on a global prediction approach. In addition, the local parameter $\mathcal{P}_{\mathrm{int}}$ showed better predictions than the J-integral parameter obtained from the same FE simulations.
- Predicting the WPS fracture load using the local parameter $\mathcal{P}_{\mathrm{int}}$ is possible without requiring FE simulations for the entire WPS cycle, as long as no WPS unloading occurs. By utilising two FE simulations of simple monotonic loading done at two different temperatures, i.e. T_{max} and T_{min}, the WPS fracture force can be estimated for the L-C-F cycle from the $\mathcal{P}_{\mathrm{int}}$ versus force plot. Such a method did not work for the L-U-C-F cycle as complications are introduced to $\mathcal{P}_{\mathrm{int}}$ due to the unloading step.

CRediT authorship contribution statement

Ahmed Azeez: Conceptualization, Methodology, Software, Formal analysis, Visualization, Writing – original draft, Writing – review & editing. **Daniel Leidermark:** Supervision, Formal analysis. **Mikael Segersäll:** Supervision, Investigation. **Robert Eriksson:** Supervision, Conceptualization, Investigation.

Declaration of competing interest

The authors declare that they have no known competing financial interests or personal relationships that could have appeared to influence the work reported in this paper.

Data availability

Data will be made available on request.

Acknowledgment

Siemens Energy AG is acknowledged for their support and providing the material used for testing.

References

[1] J. McGowan, Application of warm prestressing effects to fracture mechanics analyses of nuclear reactor vessels during severe thermal shock, Nucl. Eng. Des. 51 (1979) 431–444.
[2] BS 7910:2013+A1:2015, Guide to Methods for Assessing the Acceptability of Flaws in Metallic Structures, Standard, The British Standards Institution, 2013.
[3] H. Kordisch, R. Böschen, J. Blauel, W. Schmitt, G. Nagel, Experimental and numerical investigations of the warm-prestressing (wps) effect considering different load paths, Nucl. Eng. Des. 198 (2000) 89–96.
[4] K. Wallin, Master curve implementation of the warm pre-stress effect, Eng. Fract. Mech. 70 (2003) 2587–2602.
[5] H. Blumenauer, M. Krempe, Investigation of the warm prestress effect, Mater. Trans. 42 (2001) 85–89.
[6] B. Pickles, A. Cowan, A review of warm prestressing studies, Int. J. Press. Vessels Pip. 14 (1983) 95–131.
[7] P.A.S. Reed, J.F. Knott, Investigation of the role of residual stresses in the warm prestress (WPS) effect. Part I—experimental, Fatigue Fract. Eng. Mater. Struct. 19 (1996) 485–500.
[8] J. Chen, H. Wang, G. Wang, Z. Dong, X. Chen, Mechanism of effects of warm prestressing (WPS) on apparent toughness of notched steel specimens Part II: Calculations and analyses, Int. J. Fract. 117 (2002) 375–392.
[9] J. Chen, V. Wang, G. Wang, X. Chen, Mechanism of effects of warm prestressing on apparent toughness of precracked specimens of HSLA steels, Eng. Fract. Mech. 68 (2001) 1669–1686.
[10] M. Ayatollahi, M. Mostafavi, Effects of crack tip blunting and residual stress on a warm pre-stressed crack specimen, Comput. Mater. Sci. 37 (2006) 393–400.
[11] N. Ilchuk, L. Commin, P. Spä, G. Odette, Effect of warm pre-stressing on fracture toughness of Eurofer97 steel, Fusion Eng. Des. 88 (2013) 644–647, Proceedings of the 27th Symposium On Fusion Technology (SOFT-27); Liège, Belgium, September (2012) 24-28.
[12] C. Jacquemoud, S. Marie, M. Né, Evaluation of the active plasticity hypothesis as a relevant justification of the warm pre stressing effect, Eng. Fract. Mech. 104 (2013) 16–28.
[13] D. Van Gelderen, J. Booker, D. Smith, Evaluating the conditions when warm pre-stressing does not produce a benefit in apparent toughness, Mater. Today Proc. 2 (2015) S401–S407.
[14] P.A.S. Reed, J.F. Knott, An investigation of the warm prestressing (WPS) effect in A533B weld metal, Fatigue Fract. Eng. Mater. Struct. 15 (1992) 1251–1270.
[15] D. Van Gelderen, K. Rosahl, J. Booker, D. Smith, Monte carlo simulations of the effects of warm pre-stress on the scatter in fracture toughness, Eng. Fract. Mech. 134 (2015) 124–147.
[16] C. Jacquemoud, M. Nédélec, Loading conditions likely to modify the benefits of the warm pre stressing effect, in: ASME Proceedings of the ASME 2013 Pressure Vessels and Piping Conference. Volume 6A: Materials and Fabrication, 2013.
[17] J. Hure, C. Vaille, P. Wident, D. Moinereau, C. Landron, S. Chapuliot, C. Benhamou, B. Tanguy, Warm prestress effect on highly irradiated reactor pressure vessel steel, J. Nucl. Mater. 464 (2015) 281–293.
[18] A. Azeez, V. Norman, R. Eriksson, D. Leidermark, J. Moverare, Out-of-phase thermomechanical fatigue crack propagation in a steam turbine steel — modelling of crack closure, Int. J. Fatigue 149 (2021) 106251.
[19] A. Azeez, R. Eriksson, V. Norman, D. Leidermark, J. Moverare, The effect of dwell times and minimum temperature on out-of-phase thermomechanical fatigue crack propagation in a steam turbine steel—crack closure prediction, Int. J. Fatigue 162 (2022) 106971.
[20] K. Wallin, Warm pre-stress based pre-cracking criteria for fracture toughness testing, Eng. Fract. Mech. 71 (2004) 1737–1750.
[21] G.G. Chell, J.R. Haigh, V. Vitek, A theory of warm prestressing: experimental validation and the implications for elastic plastic failure criteria, Int. J. Fract. 17 (1981) 61–81.
[22] F.M. Beremin, A. Pineau, F. Mudry, J.-C. Devaux, Y. D'Escatha, P. Ledermann, A local criterion for cleavage fracture of a nuclear pressure vessel steel, Metall. Trans. A 14 (1983) 2277–2287.
[23] W. Lefevre, G. Barbier, R. Masson, G. Rousselier, A modified beremin model to simulate the warm pre-stress effect, Nucl. Eng. Des. 216 (2002) 27–42.
[24] A. Di Gianfrancesco, R. Blum, 24 - A-USC programs in the European union, in: A. Di Gianfrancesco (Ed.), Materials for Ultra-Supercritical and Advanced Ultra-Supercritical Power Plants, Woodhead Publishing, 2017, pp. 773–846, http://dx.doi.org/10.1016/B978-0-08-100552-1.00024-5.
[25] T.-U. Kern, M. Staubli, B. Scarlin, The European efforts in material development for 650°C USC Power Plants - COST 522, ISIJ Int. 42 (2002) 1515–1519.
[26] T.U. Kern, K.H. Mayer, B. Donth, G. Zeiler, A. Di Gianfrancesco, The European efforts in development of new high temperature rotor materials - Cost536, in: Proc. of 9th Liege Conf. on Materials for Advanced Power Engineering, Liege, Belgium, 2010, pp. 27–36.
[27] F. Abe, 10 - New martensitic steels, in: A. Di Gianfrancesco (Ed.), Materials for Ultra-Supercritical and Advanced Ultra-Supercritical Power Plants, Woodhead Publishing, 2017, pp. 323–374, http://dx.doi.org/10.1016/B978-0-08-100552-1.00010-5.
[28] S. Holdsworth, Creep resistant materials for steam turbines, in: Reference Module in Materials Science and Materials Engineering, Elsevier, 2016, http://dx.doi.org/10.1016/B978-0-12-803581-8.02063-4.
[29] G. Zeiler, 6 - martensitic steels for rotors in ultra-supercritical power plants, in: A. Di Gianfrancesco (Ed.), Materials for Ultra-Supercritical and Advanced Ultra-Supercritical Power Plants, Woodhead Publishing, 2017, pp. 143–174, http://dx.doi.org/10.1016/B978-0-08-100552-1.00006-3.
[30] R. Kaybyshev, V. Skorobogatykh, I. Shchenkova, New martensitic steels for fossil power plant: Creep resistance, Phys. Metals Metallogr. 109 (2010) 186–200.
[31] S.R. Holdsworth, Creep-fatigue properties of high temperature turbine steels, Mater. High Temp. 18 (2001) 261–265.
[32] R. Mishnev, N. Dudova, R. Kaibyshev, On the origin of the superior long-term creep resistance of a 10% Cr steel, Mater. Sci. Eng. A 713 (2018) 161–173.

[33] A. Azeez, R. Eriksson, D. Leidermark, M. Calmunger, Low cycle fatigue life modelling using finite element strain range partitioning for a steam turbine rotor steel, Theor. Appl. Fract. Mech. 107 (2020) 102510.
[34] ISO 12135:2002(E), Metallic Materials — Unified Method of Test for the Determination of Quasistatic Fracture Toughness, Standard, International Organization for Standardization, Geneva, CH, 2002.
[35] ASTM E399-12e2, Standard Test Method for Linear-Elastic Plane-Strain Fracture Toughness KIc of Metallic Materials, Standard, ASTM International, West Conshohocken, PA, 2013, http://dx.doi.org/10.1520/E0399-12E02.
[36] ABAQUS User's Manual, Version 2017, Dassault Systemes, Johnston, RI, USA, 2017.